Computational Techniques to Generate Space Launch System Aerodynamic Databases

Karen A. Deere,* Steven E. Krist,* Nalin A. Ratnayake,* Farhad Ghaffari,† Brent W. Pomeroy,* and Thomas J. Wignall‡
NASA Langley Research Center, Hampton, Virginia 23681-2199

https://doi.org/10.2514/1.A35830

This document describes the reasoning and trade studies used to evaluate tools for constructing the aerodynamic lineload databases for the liftoff and transition phases of flight for the Space Launch System. Three computational fluid dynamics codes (USM3D, FUN3D, and Kestrel) were investigated with various turbulence models as well as detached eddy simulation variants for the launch vehicle in free air and in proximity to the tower. Decisions were made mostly based on results from brief developmental studies performed in response to specific, unforeseen challenges that were encountered in the analysis of a given configuration. The need to develop databases in a timely manner, as well as to accurately capture the expected leeward-wake flowfield characteristics, led to the selection of the Kestrel flow solver with its delayed detached eddy simulation method, the Spalart–Allmaras turbulence model, and the adaptive mesh refinement capability in the off-body Cartesian grid region.

Nomenclature

C_A	=	axial force coefficient
C_l	=	rolling moment coefficient
C_m	=	pitching moment coefficient
C_N	=	normal force coefficient
C_n	=	yawing moment coefficient
C_p	=	pressure coefficient
C_Y	=	side force coefficient
dt	=	dimensional time step (Kestrel), s
dt^*	=	nondimensional time step (Kestrel)
M	=	freestream Mach number
y^+	=	nondimensional height of first cell in boundary layer
α_P	=	total angle of attack (missile axis system), deg
Δt	=	normalized time step (USM3D and FUN3D)
ϕ_P	=	aerodynamic roll angle (missile axis system), deg

I. Introduction

THE NASA Space Launch System (SLS) vehicles were designed with evolvability to provide a new launch capability for deep-space exploration [1]. The SLS variants shown in Fig. 1 consist of a common, multistage centerbody that includes the liquid-fueled main rocket engines, with two five-segment solid rocket boosters (SRBs) attached to the sides. For the Block 1 and Block 1B crewed series, the Orion crew capsule sits atop the stack. The Launch Abort System (LAS) is a shroud that covers Orion, and the LAS tower extends above it. For the Block 1B cargo variant, the LAS and Orion are replaced with a payload enclosed within a cargo fairing (CF) shroud. Figure 1 shows the three configurations of interest in the present study as well as the Block 2 Crew and Cargo variants with the evolved boosters (EBs). The SLS Block 1 configurations have a launch vehicle stage adapter (LVSA) and an interim cryogenic propulsion stage (ICPS). The SLS Block 1B and Block 2 configurations have an interstage, exploration upper stage (EUS), and a universal stage adapter (USA).

The segments of the SLS mission that are of interest for this paper are the liftoff and transition (LOT) phases of flight. This first 20 s of flight includes the rocket static on the launch pad in proximity of the tower, and up to Mach numbers M less than 0.3, where the rocket is above the tower but before the ascent phase. This low-speed flight regime is unique because the dominant loads are lateral, unlike the rest of the flight envelope where the axial loads dominate. Additionally, there is a wide range of complex aerodynamics flow features occurring at low speeds, including asymmetric vortices shed from the vehicle forebody at angles of attack α_P between 20 and 70 deg, various Coanda flow attachment states, massive flow separation above $\alpha_P = 20$ deg, and flow interactions between the rocket and tower. A combination of wind-tunnel data and computational fluid dynamics (CFD) data are ideal for understanding the complex flow around the SLS vehicle, with CFD providing force distributions along the rocket that are not easily attainable in the wind tunnel. In addition, the CFD data are beneficial for preflight risk reduction and postflight analysis.

The SLS LOT lineloads databases provide the missile-axes, six-degree-of-freedom force and moment distributed loads acting on the vehicle as a function of axial location. The databases include individual data tables for the central centerbody stage and each of the two SRBs for the vehicle on-pad, through liftoff, and then through transition to the nominal ascent trajectory. The database for a configuration is composed of two separate data sets. One data set is for liftoff, when the vehicle is in proximity to the tower, which results in significant aerodynamic interactions between the vehicle and launch tower. The second dataset is for transition, which covers the vehicle in isolation after it has cleared the launch tower, but before reaching the nominal ascent phase of flight. The SLS vehicle experiences much higher angles of attack during the transition phase of flight as the vehicle *transitions* from $\alpha_P = 90$ deg at liftoff to the near-zero angles of attack during the longer ascent phase of flight. The primary end users of the LOT lineloads databases are the Loads team and the Guidance, Navigation, and Control team at the Marshall Space Flight Center, who use the databases for sectional loading analysis and gimbal rate sensitivity analysis, respectively.

While the overall vehicle force and moment coefficients can be efficiently obtained through wind-tunnel testing, computational analyses have become indispensable for obtaining the extensive amount of surface information (i.e., distributed pressure and skin friction coefficients) required to generate accurate lineloads. Three CFD codes (USM3D, FUN3D, and Kestrel) were investigated with various turbulence models as well as detached eddy simulation (DES) variants for the launch vehicle in free air and in proximity to the tower.

The studies and decisions that have led to the best-practice procedures are documented chronologically, starting with the Block 1

Presented as Paper 2019-3399 at the AIAA Aviation 2019 Forum, Dallas, TX, June 17–21, 2019; received 28 July 2023; revision received 2 February 2024; accepted for publication 12 March 2024; published online 4 June 2024.

*Aerodynamics Research Engineer, Configuration Aerodynamics Branch. Senior Member AIAA.

†Aerodynamics Research Engineer, Configuration Aerodynamics Branch. Associate Fellow AIAA.

‡Aerodynamics Research Engineer, Configuration Aerodynamics Branch.

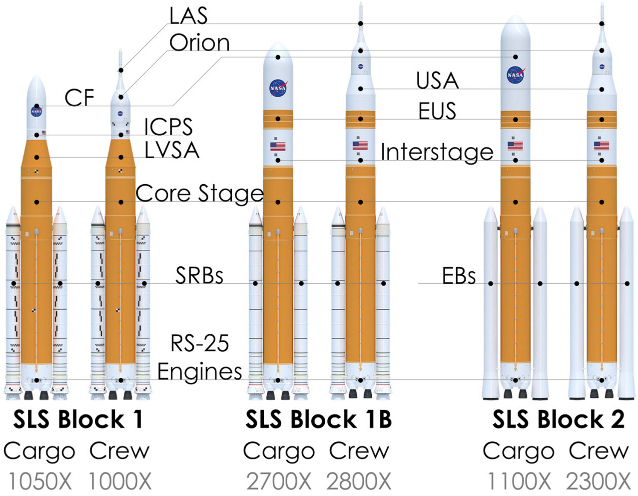

Fig. 1 The SLS configurations (source: NASA/Michael W. Lee 968.0).

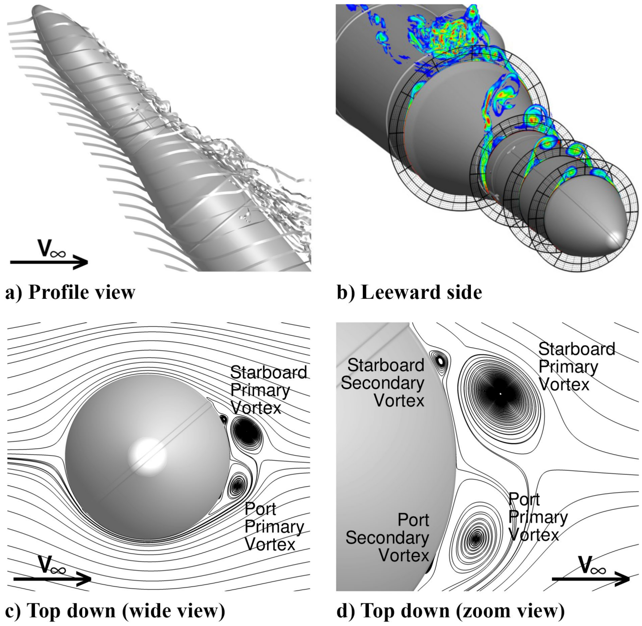

Fig. 2 Separated flowfield showing primary and secondary asymmetric vortices [5].

Crew, followed by the Block 1B Cargo, and conclude with the Block 1B Crew vehicle with and without the launch tower. The best practice procedures will be applied to the Block 2 Crew and Cargo variants for future databases.

A. Aerodynamic Considerations for LOT Problem

Aerodynamic conditions associated with the LOT regime involve low-speed flow ($M < 0.3$), at total angles of attack ranging from $\alpha_P = 0$ deg to $\alpha_P = 90$ deg for vehicle roll angles ϕ_P from $\phi_P = 0$ deg to $\phi_P = 360$ deg. For $\alpha_P \gtrapprox 30$ deg, the flow exhibits significant leeward separation from the sides of the vehicle; the effects of the resultant large trailing wakes on the leeward surface pressure field were difficult to capture accurately in computational simulations. In addition to such low-speed flow relative to the velocities in other SLS flight regimes, the LOT regime poses unique challenges for experimental and computational investigations due to the extreme angles of attack at various vehicle roll angles. Moreover, a number of complex phenomena arise over the course of the transition through the intermediate angles of attack, including the evolution of asymmetric vortex systems and the influence of Coanda effects on the flow through the gaps between the SRBs and the centerbody; both of these phenomena are extremely sensitive to small changes in orientation and geometry.

For vehicles with slender forebodies, large, stable asymmetric vortices can be generated at midrange angles of attack [2–5]. Figure 2 shows a separated flowfield from a forebody with primary and secondary asymmetric vortices. The vortex on one side of the forebody will remain close to the body, while the vortex on the opposite side of the symmetry plane rises away from the body or may collapse altogether. Figure 2a shows the profile view of the vortices on the leeward side of the body, while Fig. 2b shows a top view of the leeward side where it is more noticeable how one vortex rises up farther away from the body than the other. It is interesting that the vortex close to the surface is more coherent, but the vortex farthest from the surface appears to be just as strong. The effect of the phenomena is to induce a side force of significant magnitude on the forebody, which could appear even when the body is symmetric and/or at zero sideslip angle. Moreover, the orientation of the vortex system may switch from one side to the other on repeated instances at the same condition, as the vortex formation is extremely sensitive to minor differences in geometric features and flow conditions. This repeated vortex switching for a single configuration at a set wind-tunnel condition has occurred [6,7], and the conditions are generally avoided to prevent damage to the balance within the model. Although the flowfield for the asymmetric vortex system is unsteady, for most configurations, the vortex pattern is stable on one side of the forebody during computational runs, as the length of the simulation is but a few seconds [4].

None of the SLS configurations were geometrically symmetric, due to the presence of protuberances that were positioned nonuniformly over the vehicle. All variants of the SLS vehicle exhibited asymmetric vortex behavior ranging from $\alpha_P = 20$ deg to $\alpha_P = 70$ deg.

The orientation of the asymmetric vortices can cause not only a large change in the magnitude of the side force but also a change in the sign. In computations, minor perturbations to parameters, such as the exact mesh geometry or solver settings, have affected the directionality of the asymmetry [8], raising the qualitative uncertainty in lateral loading. Comparisons between experimental and computational results for side force were generally poor unless the computation captured the same orientation of the asymmetric vortices as what was observed in the experiment.

Much like the situation for the asymmetric vortices, the Coanda effect exhibited in the regions around the gaps between the SRBs and the centerbody was extremely sensitive to geometry; flow conditions, and, in numerical simulations, the mesh geometry and flow solver parameters. The Coanda effect has been well characterized both analytically and experimentally in the literature and was described well by Levinsky and Yeh [9]. For the SLS vehicles during LOT, the Coanda effect was bistable (two equilibrium states) where the attached flow on the leeward side of the gaps had a tendency to wrap around either the centerbody or the SRBs. If the flow wrapped around the SRB, then the increased velocity generated more negative pressure coefficient values on the leeward side of the SRB and more positive values on the leeward side of the centerbody, with the reverse being true if the flow wrapped around the centerbody. Numerical simulations of SLS configurations suggest that the Coanda effect was present from $\alpha_P = 15$ deg (the lowest angle of attack for which simulations were run) through $\alpha_P = 90$ deg. Because bistable flow can occur between each of the two gaps between the SRBs and the centerbody, the Coanda effect can produce four states at a given axial location along the length of the SLS launch vehicle.

Figure 3 shows four possible Coanda states for the flow around the leeward side of both gaps for flow that approached the SLS vehicle at $\alpha_P = 90$ deg and $\phi_P = 0$ deg. Figure 3 shows a top down view of a three-body rocket, with flow moving from the bottom to the top of the figure as if the flow is perpendicular to the height of the rocket. Figure 3a shows the flow bent to the left and attached to the starboard sides of the port SRB and the centerbody. Figure 3b shows the flow bent to the right and attached to the port sides of the centerbody and the starboard SRB. Figure 3c shows the flow bent around and attached to both sides of the centerbody. Finally, Fig. 3d shows the flow bent around and attached to both SRBs. Additionally, multiple Coanda states may occur at different axial locations along the length of the

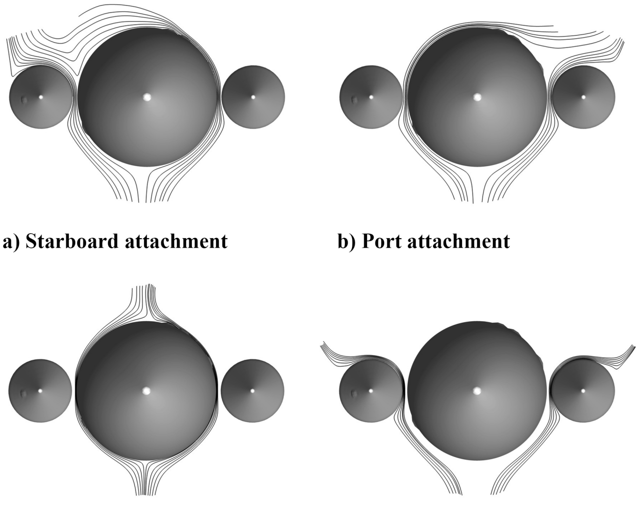

Fig. 3 Four Coanda states [5].

vehicle or at nonzero roll angles. For instance, at $\phi_P = 60$ deg, the starboard SRB was upstream of the centerbody yet still exhibited the Coanda effect, but because the port SRB resided entirely within the wake of the centerbody, there was no significant flow through the gap between the port SRB and centerbody. Moreover, for roll angles near $\phi_P = 90$ deg and $\phi_P = 270$ deg, there was no significant flow through either of the gaps between the SRBs and centerbody. Finally, as the angle of attack approached $\alpha_P = 0$ deg, the Coanda effect faded away for all roll angles.

Although a number of lateral loading possibilities exist for some of the flow conditions, the influence of the various Coanda states on the magnitude of the forces and moments was not nearly as large as that of the orientation of the asymmetric vortices. Nevertheless, the Coanda state had a significant effect on the lineloads for the SRBs and the centerbody, and it was relatively easy to discern whether a CFD result captured the same Coanda flow attachment that was captured in the wind tunnel through comparison of the pressure coefficients at the experimental pressure tap locations.

The challenges were compounded for the liftoff phase of flight with the addition of the SLS launch tower into the flow domain, which produced significant interference effects upon the vehicle's aerodynamic forces and moments [10]. The launch tower apparatus was attached to a turntable such that testing was conducted through a 330 deg range in wind azimuth angle. Given the limits of the test setup, all wind-tunnel testing and computations for the liftoff phase of flight were conducted at $\alpha_P = 90$ deg. Particular challenges and decisions associated with the launch tower CFD gridding and solution development were described in Ref. [11]. Finally, Ref. [7] provided evidence from a recent 14-by 22-Foot Subsonic Wind Tunnel (14×22 WT) test confirming the bistable nature of the flow through the gaps between the SRBs that was caused by the Coanda effect.

B. Computational Considerations for LOT Problem

The fundamental difficulty in numerical simulations for the LOT flight regime was accurately capturing the effects of large wakes on the pressure field about the leeward surface of the vehicle. It has long been common knowledge in the CFD community that Reynolds-averaged Navier–Stokes (RANS) solutions may not capture smooth-surface flow separation or the resulting wake [12]. The LOT regime encompassed conditions with very high angles of attack, and numerical simulations of this problem demanded the employment of schemes that were more complex than RANS methods. Because the application of large eddy simulation (LES) methods to LOT problems remains infeasible, it was necessary to resort to hybrid RANS/LES methods, such as DES methods and its many variants, including delayed DES (DDES), modified DDES (MDDES) and improved DDES (IDDES). As described by Spalart [13], these hybrid methods essentially involve using RANS methods in the boundary layer region and LES-like methods for the extended wake. Although the original DES method was based on the Spalart–Allmaras (SA) turbulence model [14], DES variants can be used with any turbulence model that makes use of a properly defined length scale. However, the computational grid must be sufficiently refined on the leeward side of the vehicle in order to adequately capture the small eddy content of the wake, requiring more memory resources and time steps than needed for RANS methods.

The first set of solutions to the SLS transition problem was obtained with the USM3D CFD code [15]. Exposure to the resource requirements of the USM3D DES simulations for the transition problem, along with the expectation of even higher costs for the liftoff problem, led to evaluation of the FUN3D [16] and Kestrel [17] flow solvers, both of which had the option for implementing DDES methods on unstructured mixed-element grids.

The CFD simulations reported herein were executed at the NASA Advanced Supercomputing (NAS) facility located at the NASA Ames Research Center. Depending on the configuration and gridding approach, meshes ranged from 0.5 to 3.5 billion grid points. Simulations were executed on 500 to 2500 cores and required 1 to 10 days of compute time. With such expensive resource demands, solution development efficiency at all points in the CFD workflow, from gridding to numerical simulation to postprocessing, while still maintaining acceptable accuracy, was of paramount concern in the selection of tools.

C. CFD Codes

The USM3D flow solver was originally developed at the NASA Langley Research Center (LaRC) as part of the Tetrahedral Unstructured Software System (TetrUSS) software system. USM3D has been applied to and validated on a wide array of aerodynamic problems over the course of approximately two decades [18]. USM3D is a finite volume, cell-centered method for solving the Euler and RANS equations on tetrahedral unstructured grids. In addition to the traditional RANS capability, USM3D provides an implementation of DES and supports a variety of turbulence models for closure of the Navier–Stokes equations.

The FUN3D [16] flow solver, developed and maintained at NASA LaRC, is well known for its design optimization, propulsion, and thermodynamic model capabilities with applications spanning from incompressible flows up to the hypersonic regime [16]. FUN3D is a node-centered method for solving the Euler and RANS equations in both the incompressible and compressible forms. Both standard tetrahedral grids and mixed-element unstructured meshes with arbitrary combinations of tetrahedra, prisms, and pyramids can be used with FUN3D. In addition to traditional RANS capability, FUN3D supports DES, DDES, and MDDES methods in conjunction with a number of variants of SA and two-equation turbulence models.

The Kestrel [17] flow solver was developed and is maintained by the Computational Research and Engineering Acquisition Tools and Environment, Air Vehicles (CREATE-AV) project under the U.S. Department of Defense (DOD) High-Performance Computing Modernization Program. Kestrel is a finite volume, cell-centered, unstructured flow solver. Of particular interest to the team was the dual mesh flow solver methodology, in which the computational domain was divided into near-body and off-body domains, and the adaptive mesh refinement (AMR) capability. The near-body flow was computed on an unstructured grid that encapsulates the solid body, and this near-body grid was surrounded by a Cartesian mesh that extends to the far field. An example of the dual mesh approach, with an orange unstructured inner grid and gray outer Cartesian grid, is shown in Fig. 21 of Ref. [5]. For this work, the inner unstructured grid has triangles on the surface, prisms in the boundary layer, and tetrahedra outside of the boundary layer. In addition to traditional RANS capability, Kestrel had the option for DDES at the time of this work but has since implemented the IDDES method.

D. Lineloads Database Development Workflow

Computational simulations were necessary for coupling experimental wind-tunnel results with a mathematical reduced-order model

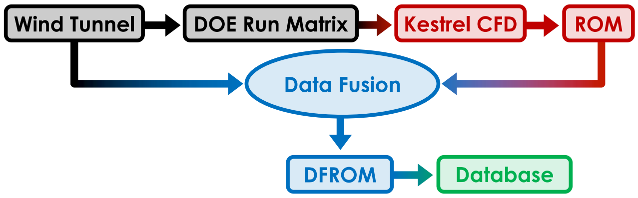

Fig. 4 LOT lineloads database development workflow [5].

(ROM). The nominal workflow is shown in Fig. 4, where CFD was performed for a limited set of wind-tunnel flow conditions determined by a design of experiments (DoF) study to provide the optimal subset of information in the desired lineload database space. The surface pressure and skin friction surfaces from the CFD were then used to train a ROM, which used the modal information in the CFD solutions to generate an interpolated, multidimensional space of surfaces across all points in the desired database range. Such surfaces from the ROM can be integrated to derive lineloads at flow conditions where no CFD solutions were obtained. The power of the ROM was significant with approximately 70 CFD simulations used in the workflow that produced 450 database points.

To improve the accuracy of the model, the ROM forces and moments were anchored to wind-tunnel measured data, which allowed for corrections that created a data-fused reduced-order model (DFROM). The DFROM lineload coefficients as a function of body station were finally transformed into the desired coordinate system (usually body axis) and tabulated at all desired database breakpoints. Details on the methodology and development of the ROM and DFROM are described in Ref. [19].

II. SLS Block 1 Crew (2014-2015)

The first SLS configuration for which LOT lineloads were developed was the Block 1 Crew configuration from design and analysis cycle 2 (DAC2). The outer mold line (OML) for the CFD model of the SLS Block 1 Crew configuration, which was similar to the definition for the wind-tunnel model, is shown in Fig. 5. The metric portion of the vehicle, upon which integrated forces and moments were measured, included the centerbody from the top of the LAS to the termination of the nozzle aerodynamic fairings and the SRBs from the conical fairing at the top to the base of the SRB nozzles (purple and magenta surfaces). The measured forces and moments did not include the black base surfaces, the cavity, or the sting. While the model of this configuration was quite complex, it did not include many of the features included in subsequent models, such as the numerous structural support rings on the SRBs, the brackets on the feedlines, and a host of small protuberances.

Because of the complexity of the SLS launch vehicle OML, an unstructured grid approach was chosen for the CFD analysis. Moreover, for the five years immediately preceding the SLS program, the LaRC SLS CFD Team had been using the TetrUSS suite of tools to construct aerodynamic databases for the LOT and ascent regimes of the Ares I-X and Ares I launch vehicles as part of the NASA Constellation Program [20,21]. Hence, the selection of USM3D as the flow solver was a natural initial choice for this complex problem. The initial strategy used in developing the grids and setting the input parameters for USM3D was based upon the best-practice procedures for analyzing the aerodynamic characteristics of the Ares-I family of launch vehicles [22]. Although these procedures were useful, the Ares I-X and Ares I launch vehicles were single-stack rockets, while the three-body SLS launch vehicle with two SRBs inherently have additional flow phenomenon to consider. To further develop the best-practices appropriate for DES computations, before tackling the complexity of the SLS configuration, a series of DES computations were conducted on a circular cylinder and then on a simplified Titan III configuration.

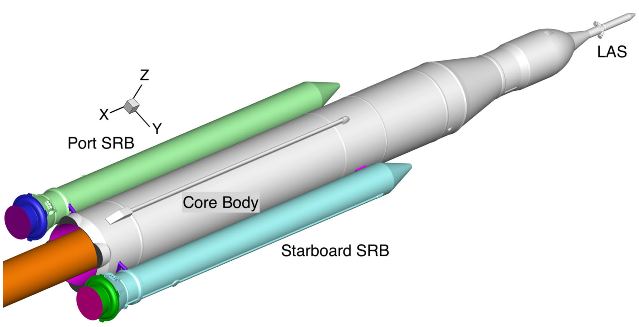

Fig. 5 The CFD OML for the SLS Block 1 Crew configuration.

A. Titan III Studies

Similar to the SLS launch vehicle, the Titan III commercial launch vehicle is a three-body configuration, making it a suitable candidate for studying interaction effects that were unnecessary for the single-body Ares-I configuration. Experimental force and moment data, along with limited pressure data, were available at liftoff conditions, providing validation data for the simulations. Moreover, the simplified Titan III geometry provided a much cleaner, and thus less resource-intensive simulation than that for the SLS configurations. The geometry further bolsters the argument to use the Titan III as a test case for methods development. Applying the best practices that were current at the time, USM3D runs used a second-order accurate spatial discretization with Roe's flux-difference splitting scheme for the inviscid fluxes. All computations were run in time-accurate mode because significant regions of the flow were expected to be unsteady for most of the conditions within the LOT flight envelope. The second-order time-accurate differencing scheme with the pseudotime variable was employed.

Three commonly used turbulence models in aircraft and spacecraft aerodynamic assessments are the one-equation SA model, the two-equation k-ϵ model, and the two-equation Menter shear-stress transport (SST) model. The smaller resource requirements of the Titan III problem allowed for timely investigations into refinements of the gridding procedures, the generation of temporal and spatial resolution studies, and the assessment of the SA, SST, and k-ϵ turbulence models, within both the RANS and the DES modes of computations. Results from the Titan studies indicated that RANS solutions were only adequate up to angles of attack less than 20 deg; at higher angles of attack, the RANS simulations overpredicted the suction in the massively separated wake, whereas the DES mode provided results that were more aligned with experimental values. While all three turbulence models performed adequately in both the RANS and DES modes, the k-ϵ turbulence model was found to produce results that were marginally more in line with experimental results than the SA and SST models. The Titan III studies also yielded new guidelines for gridding the SLS configuration, which are discussed in Sec. II.B.

B. SLS Block 1 Crew Grid Development

Generation of the unstructured tetrahedral grids for USM3D was performed with the TetrUSS utilities GridTool, VGRID, and POSTGRID. The grid generation process began with the importation of the CAD geometry into GridTool, where surface patches covering the entire OML were defined and grouped to form components. Of primary importance in generating accurate solutions was the source specification, as the grid spacing and local density of the cells was related to the strengths and locations of the sources, which allowed the user to refine the grid in regions of high flowfield gradients. Line sources with anisotropic stretching were deployed on the OML around regions where components intersected and where sharp discontinuities in the OML surface existed, which allowed for the efficient capture of surface discontinuities with elongated cells. As the elongated cells grew from the surface to the far field, the skewness was reduced, and the volume in the cell increased through the boundary layer with increasing distance from the wall. The hybrid DES method employed RANS modeling in this region of the grid, near the surface, which worked well for the anisotropic cells. In contrast, the LES solver in the DES method preferred isotropic cells, but the switch from RANS to DES occurred at some distance away from the walls, preferably at the outer edge of the boundary layer. Volume sources in the shape of a cylinder, cone, or sphere were sized to envelope the larger components of the vehicle and extended a significant normal distance beyond the OML surfaces. The source specifications for the volume sources were specified to generate isotropic cells. The line sources dominated near the surface and the volume sources dominated outside the boundary layer. Therefore, the cell structure moving from the OML surface, out through the boundary layer, transitioned from anisotropic cells on the surface to the isotropic cells required by LES methods, as quickly as practicable. The GridTool geometry was imported to VGRID, which employed a three-step process to generate an unstructured volume mesh composed of tetrahedra. The first step generated a surface triangulation, the local resolution of which was controlled by the source specification. The second step employed an advancing layer method to grow a boundary-layer grid normal to the surface. The spacing for the height of the first layer of cells off the wall was set and confirmed that y^+ values over the entire surface of the vehicle remained lower than 1.0. The third step employed an advancing front method to discretize the inviscid flow region. Finally, the POSTGRID utility was used to close holes in the volume grid left by the VGRID process.

Further strategies for appropriately specifying the source strengths and distributions were developed through a grid resolution study of the Titan III. Of particular importance was the determination of the representative cell size that was applied to the isometric gridding of the wake. The Titan III study was also used to size the radius of the volume sources in the wakes.

The only significant difference in generating grids for RANS and DES simulations was how the resolution in the wake region was treated. For the DES method, a highly refined mesh in the wake region was necessary but was not beneficial for the RANS method. It was necessary to create separate meshes for RANS and DES simulations, and to generate separate meshes for each roll angle for the DES simulations, because the finely-resolved wake regions for DES that require additional resources are unnecessary for RANS simulations. Therefore, one mesh was used for the RANS simulations with no attempt to resolve the wake regions, and all the volume sources were defined within the OML surface. For the DES simulations, the volume sources were extended well out into the flowfield on the leeward side of the vehicle to provide sufficiently fine resolution in the wake region for each roll angle. The effect of skewing the volume sources in order to appropriately position the refined wake for a specified roll angle is shown in Fig. 6, in which cross-sections of the grid through the centerbody and SRBs are shown for the RANS grid and the DES grid for a roll angle of 60 deg. Note that the grid spacing from the SRB wake sources was finer than that from the centerbody wake source and overrides the centerbody source influence in the region of overlap.

The RANS grid was composed of 186 million cells, which was about 20% larger than the grids typically generated for ascent analyses of SLS configurations with a substantially larger numbers of protuberances. The DES grids ranged from 438 million to 460 million cells, depending on the roll angle. The grids represent what was considered a medium level of refinement in a grid study.

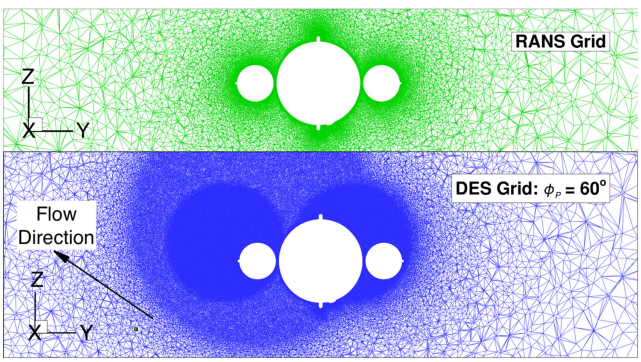

Fig. 6 Cross-sections of the unstructured RANS grid and the DES grid for the SLS Block 1 Crew configuration at $\phi_P = 60$ deg.

C. USM3D Results for SLS Block 1 Crew

The approach developed from the Titan III study was applied directly to the setup for the SLS Block 1 Crew transition problem. The run matrix was composed of five RANS cases run at $\alpha_P = 0$ and 10 deg and 16 DES cases run at $\alpha_P = 30, 55, 70,$ and 90 deg, with roll angles at $\phi_P = 0, 30, 60,$ and 90 deg; all cases used the k-ϵ turbulence model. The computational results were obtained at wind-tunnel conditions of $M = 0.183$ at a Reynolds number of 615,000 based on the nominal centerbody diameter.

The solutions were run at a normalized time step of $\Delta t = 8.0$, using 10 subiterations per time step. Normalized time steps for the Kestrel runs differed from that value, as the governing equations for Kestrel were normalized differently than those for USM3D and FUN3D. A more universal appraisal of the time step was to compute how many time steps it takes a particle traveling at freestream conditions to travel the characteristic length of the problem. For the liftoff problem, where total alpha was at 90 deg, the characteristic length was the diameter of the centerbody. For the transition portion of the database, the characteristic length increases as the total alpha decreases, but it was not clear what that length should be; consequently, the same time step was used for all angles of attack. A perusal of the literature suggests that anywhere from 100 to 800 time steps to travel the characteristic length was appropriate. For the number of runs needed in the databases, it was determined that 200 time steps was about all that could be afforded, and then a condition with smaller time steps was run to see if there was a significant difference in the results; there was not.

Given a five-day limit on each supercomputer job and the typical request for 1200 processors, each job was limited to approximately 16,000 time steps. While the residuals of the time-dependent solutions were converged for each time step, there was no expectation of obtaining converged force and moment histories; instead, time histories of the integrated forces and moments plateau and the subsequent trends can be characterized as having reached a statistical steady state, as the values oscillate about some pseudomean value. Once a statistical steady state was reached, the time-averaging procedures within the code were invoked, and the solutions were run additional time steps over which time-averaged values of the force and moment coefficients and surface and volume flow properties were computed. For the SLS Block 1 Crew configuration, 20,000 to 40,000 time steps were typically required to reach a statistical steady state, with the higher angles of attack taking longest to reach that state. The time-averaging window was set at 4000 time steps, which yielded a time-averaging window that was 2 s in duration in real time.

An indication of the quality of results obtained with USM3D is provided in Fig. 7, in which comparisons of the force and moment coefficients for a pitch sweep at a roll angle of 0 deg between CFD simulations and the wind-tunnel force and moment database are shown. The C_l, C_Y, and C_n coefficients were also plotted with the opposite y sign and marked as USM3D DES k-ε $(-y)$ in the legend to include the potential cases where the asymmetric vortices set up on the opposite side as the computed CFD results. The magnitudes of the coefficients were not included because of International Traffic in Arms Regulations (ITAR) restrictions. However, as an aid in understanding the data trends, a horizontal line was provided at the zero value of the coefficient with positive values above zero. Further, the ranges of the vertical axes for the normal and side force were the same, as were those for the pitching and yawing moment. The error bars shown on the open circles indicate the wind-tunnel force and moment database uncertainty. Note the large magnitude of the error bars between $\alpha_P = 20$ deg and $\alpha_P = 50$ deg, which reflects the scarcity of data in this region due to model dynamics issues.

Good agreement was observed between the CFD results and the wind-tunnel data in Fig. 7, especially when including the USM3D DES k-ε $(-y)$ data. Trends and magnitudes in the normal force and pitching moment, which were by far the largest coefficients at this orientation, were well captured by the USM3D DES k-ε data. Nonetheless, the coefficient values for $\alpha_P = 55$ deg and above were at the outer edge of the wind-tunnel database error bars. For the side force and yawing moment coefficients, the wind-tunnel values remained near zero up to $\alpha_P = 20$ deg, after which the values were positive,

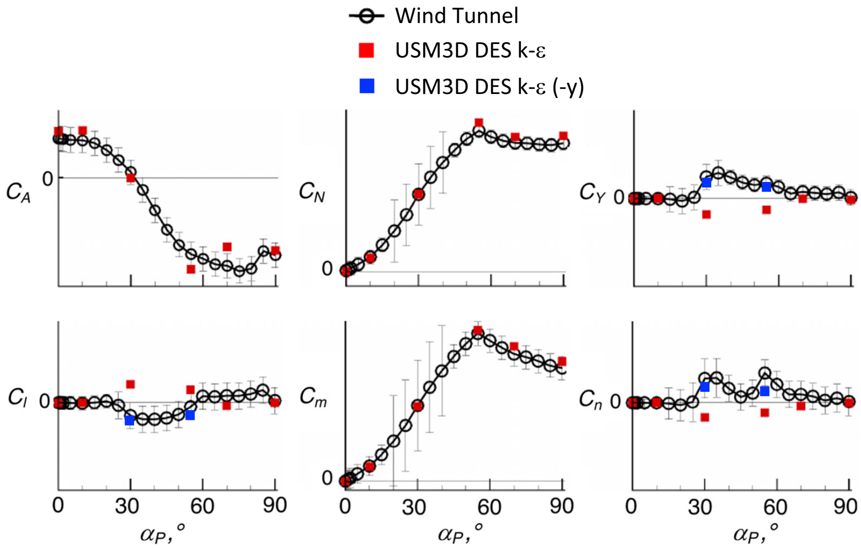

Fig. 7 Coefficient comparisons between the wind-tunnel and USM3D DES k-ϵ data for the SLS Block 1 Crew configuration at $M = 0.183$ and $\phi_P = 0$ deg for the computed and the reversed data in the $-y$ coordinate.

gaining significant magnitude and eventually decreased back to zero by $\alpha_P = 90$ deg. The USM3D DES k-ε data for the lateral coefficients had the opposite sign and were slightly underpredicted compared to the wind-tunnel values; however, the USM3D DES k-ε $(-y)$ data fall within the experimental uncertainty bands. The difference between CFD and wind-tunnel data for the lateral coefficient values with increased angle of attack was attributed to the asymmetric vortices. As discussed in Sec. I.A, the directionality of the asymmetric vortices was known to be stochastic, and therefore, if the CFD captured the vortices of the opposite orientation that was realized in the experiment, the comparison to wind-tunnel data was poor. However, such data discrepancies do not indicate a flaw in the CFD result but rather an opportunity to capture multiple states of the flow that can occur on the rocket forebody. The approach to account for the discrepancy between experiment and CFD data was to provide alternate lineloads that included both asymmetric vortex states in the database. This was deemed superior to providing single lineloads with large uncertainty bands at the conditions where multiple states occur.

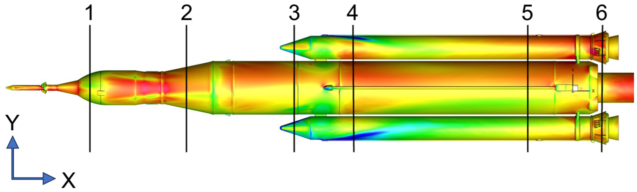

Fig. 8 Stations 1–6 and C_p on the leeward surface of the SLS Block 1 Crew configuration, USM3D DES k-ϵ at $M = 0.183$, $\alpha_P = 30$ deg, and $\phi_P = 0$ deg.

An example in which the asymmetric vortices observed in the CFD had the opposite orientation from that which was captured in the wind tunnel was at the condition of $\alpha_P = 30$ deg and $\phi_P = 0$ deg. Thus, by plotting the CFD with $(-y)$ for C_Y, C_l, and C_n in Fig. 7, it was shown that the $(-y)$ results fall within the experimental uncertainty band. Figures 8 and 9 show the flow contours from USM3D DES k-ε for this condition. Figure 8 shows the C_P contours on the leeward surface, with red contours indicating positive pressure coefficient values and blue contours indicating negative values of pressure coefficient. While the pressures were largely symmetric from the nose through station 1, by station 2, the pressures were distinctly asymmetric. At station 3, the flow was no longer symmetric across the $y = 0$ plane, and there was clearly more suction on the port SRB indicated by a larger streak of blue contours than on the starboard SRB. Figure 9 shows M contours at various axial stations, with the port SRB on the left, the starboard SRB on the right, and with the lowest M indicated by blue contours. The primary and secondary vortices discussed in Fig. 2 were present at stations 2–3. The primary vortex above the port SRB was strong and organized by the time it reached midway between stations 4 and 5, and there was a larger region of high M contour values (red) wrapped around the port SRB than on the starboard SRB. The suction from the strong vortex above the port SRB increased the strength of the Coanda flow around the

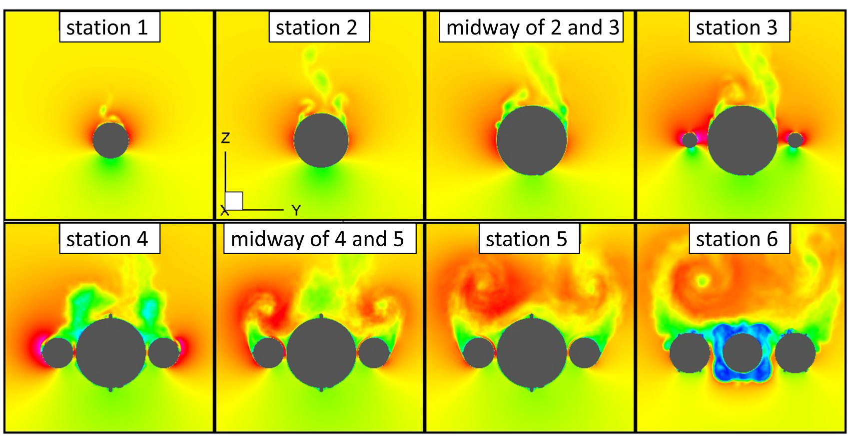

Fig. 9 Mach contours at stations 1–6 for the SLS Block 1 Crew configuration, USM3D DES k-ϵ at $M = 0.183$, $\alpha_P = 30$ deg, and $\phi_P = 0$ deg.

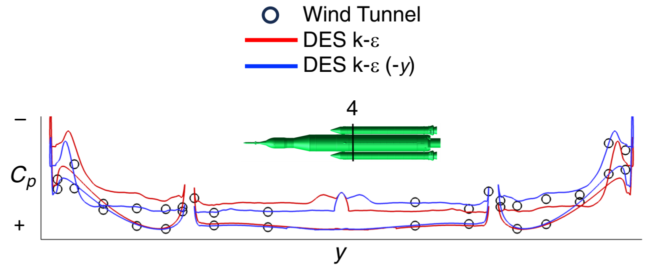

Fig. 10 Comparison of C_p between wind-tunnel and USM3D DES k-ϵ data for the SLS Block 1 Crew configuration at $M = 0.183$, $\alpha_P = 30$ deg, and $\phi_P = 0$ deg for the computed and the reversed data in the $-y$ coordinate.

port SRB. This may be the first recognition that the asymmetric vortices had an influence on the Coanda flow.

Another set of wind-tunnel data that was used to validate the CFD results was the static pressure data, which were taken at 150 pressure ports located on the wind-tunnel model centerbody and SRBs. The cross-sections at which the groups of pressure ports were located are shown at the stations in Fig. 8. An additional line of pressure ports (not shown) was taken longitudinally along the centerbody at a clock angle of 30 deg from the y axis; for this particular view, the line of ports appeared along the starboard side of the centerbody. The flow asymmetry was confirmed in the plot of the wind tunnel and time-averaged CFD pressure coefficient data for station 4 at $\alpha_P = 30$ deg and $\phi_P = 0$ deg, shown in Fig. 10. In this plot, the view is looking forward with the port SRB on the left and the starboard SRB on the right. The aerodynamic convention for plotting the pressure coefficient was employed, with the vertical axis direction reversed from the usual orientation, with higher values on the axis indicating lower pressure. The wind-tunnel data are shown with the black open circles, red lines show the actual CFD values, and blue lines show the CFD values plotted against the negative values of the y coordinate, thereby giving an estimate of what the CFD pressures would have been if the CFD had captured the same orientation of the asymmetric vortices exhibited in the wind-tunnel test. The actual CFD results were poorly correlated with the wind-tunnel values; however, very good agreement with the wind-tunnel data was obtained when the y coordinate of the CFD data was reversed.

More extensive results from the initial CFD study of the Block 1 Crew vehicle at liftoff conditions were published in Ref. [23], which contains additional comparisons of the CFD results to data taken from the LaRC 14 × 22 WT test for this configuration (Test 609). The conclusion from that study was that the USM3D results were in good agreement with the wind-tunnel data as long as the CFD simulation captured the same asymmetric vortex and/or Coanda state as the wind-tunnel experiment. Otherwise, the agreement was only moderately good. Fortunately, the USM3D results were deemed to be sufficient for this application, but only because the development of a state-of-the-art DFROM made it possible to synthesize the CFD generated spatial information at the various conditions with wind-tunnel data to provide corrected lineloads across the flight regime.

III. Methods Refinement Following Block 1 Analysis Cycle (2016)

Before undertaking the job of generating databases for the two Block 1B configurations, a number of studies were initiated to improve upon the existing SLS LOT workflow. While the accuracy of the results obtained using USM3D for the Block 1 vehicle was sufficient, the time needed to develop an aerodynamic database in the program environment was deemed unacceptable. This included both time to prepare a suitable mesh as well as the large computational cost of such a simulation. Furthermore, USM3D did not yet support a functional implementation of the DDES method at the time, which was considered a deficiency. As discussed in Ref. [13], inherent limitations with DES for certain classes of problems can be overcome with implementations of DDES and other variants of hybrid RANS/LES methods.

As discussed next, additional studies to decrease the time to get a solution of the LOT problem with USM3D were not particularly successful, so the decision was made to search for an alternative flow solver. The two alternative solvers that were evaluated were FUN3D and Kestrel, described in the following subsections. The primary reason for selecting these two flow solvers was that FUN3D and Kestrel used mixed-element unstructured grids, provided existing DDES capability, and had significant support groups working constantly to keep the codes up to date in terms of both flow solver features and maximizing the speed with which they run on state-of-the-art computer clusters.

A. Additional Investigations with USM3D

Several representative cases were run with USM3D using the k-ϵ turbulence model with both the RANS and DES methods. As expected, DES provided significantly better correlation to the database force and moment data and wind-tunnel surface pressures than the RANS approach, particularly on the leeward side of the vehicle.

The choice of turbulence model was reexamined because the selection of the k-ϵ model over the SA and SST models was based on results from the Titan III studies. Therefore, a series of DES simulations with the three turbulence models were computed at a roll angle of 0 deg on the SLS Block 2 Crew OML. The integrated force and moment results were similar, with the largest difference of 8%. A comparison of the pressure coefficient between the three turbulence models and wind-tunnel data for the $\alpha_P = 70$ deg case is shown in Figs. 11 and 12 for station 5 and along the length of the centerbody for $\phi = 30$ deg, respectively.

The main distinguishable difference at station 5 was on the port SRB and centerbody due to the SST simulation capturing a Coanda flow attached to the port side of the centerbody, while the SA and k-ϵ models captured the Coanda flow attached to the port SRB. There was good agreement in C_p between the turbulence models except in the region where the OML transitioned from the Orion diameter to that of the centerbody; the k-ϵ model predicted a larger expansion of the flow than the SA or SST turbulence models.

Ultimately, the team concluded that the difference in validity of the solution between the three turbulence models, as applied to the SLS

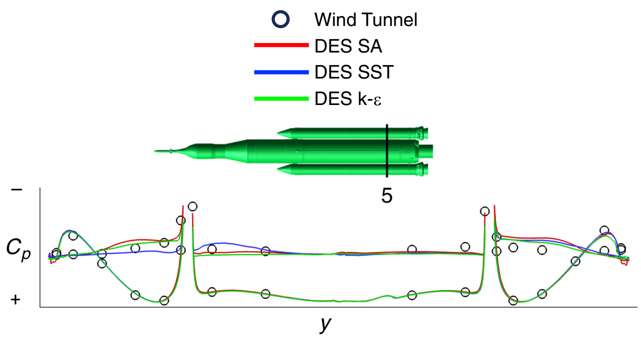

Fig. 11 Effect of USM3D turbulence model on C_p and comparison to wind-tunnel data for station 5 on the SLS Block 1 Crew configuration at $M = 0.183$ and $\alpha_P = 70$ deg.

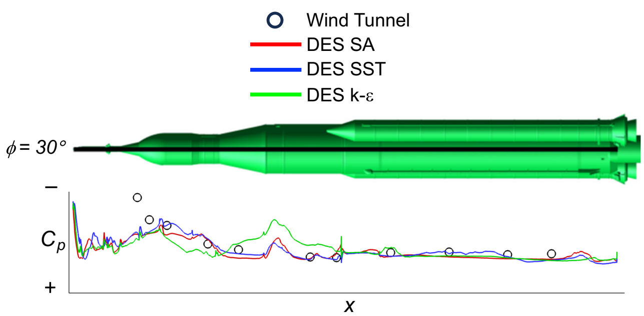

Fig. 12 Effect of USM3D turbulence model on C_p and comparison to wind-tunnel data for $\phi = 30$ deg on the SLS Block 1 Crew configuration at $M = 0.183$ and $\alpha_P = 70$ deg.

Table 1 **Computational resource requirements for the SLS Block 1 Crew DAC2 LOT application**

Flow solver	Cell type	Nodes ($\times 10^6$)	Cells ($\times 10^6$)	Turbulence model	Elapsed Real Time, h
USM3D ($\Delta t = 8$ for all time steps)	Tetrahedra	78	460	DES k-ϵ	300–600
USM3D ($\Delta t = 40$ for 2000 time steps, $\Delta t = 8$ to the end)	Tetrahedra	78	460	DES k-ϵ	180–360
FUN3D (incompressible)	Tetrahedra	122	717	DDES SA	102
FUN3D	Tetrahedra	122	717	DDES SA	135
FUN3D	Mixed	122	489	DDES SA	189
Kestrel (NAS, version 7)	Mixed	1100	100	DDES SA	99
Kestrel (Eglin, version 8)	Mixed	1100	100	DDES SA	46

Block 1 Crew configuration, was negligible. This was a surprising conclusion because the Titan III results were very sensitive to the choice of turbulence model. It was conjectured that the improved correlation of the three models on the SLS configuration was due to the influence of the protuberances on the SLS. In particular, at the 0 deg roll angle that was assessed, systems tunnels on the outboard sides of the SRBs were likely to fix the location of the separation at the same position for all three turbulence models, whereas the Titan III model had no protuberances at these critical locations. In the end, the study led to a preference for the SA model because, as a one-equation model, it was more resource efficient than the other two turbulence models.

The primary deficiency of USM3D for the LOT problem was that the supercomputer resource requirements were simply too large to run the number of simulations required to complete a database. Specifically, simulations simply required too many time steps to reach a statistical steady state. Hence, a study was initiated in an attempt to accelerate the solution progression. A two-step approach that resulted in significant time savings was to first start a solution with a much larger time step ($\Delta t = 40$) for the first 2000 time steps to initialize the solution to the flow conditions, and then second, revert to the smaller time step ($\Delta t = 8$) for the rest of the run. This two-step approach yielded run times that were around two-thirds that of the original runs ($\Delta t = 8$ for all time steps); see Table 1. Subsequent solutions from Kestrel demonstrated that the codes were fairly equivalent in the amount of time required for each time step, but Kestrel solutions reached a statistical steady state with half as many time steps as USM3D, yielding a 45% reduction in resource requirements over the fastest USM3D runs.

B. Evaluation of FUN3D

In comparing the FUN3D and USM3D results, it is important to bear in mind the differences between the node-centered FUN3D solver and the cell-centered USM3D solver. For the DES grid constructed for a roll angle of 0 deg, the computational grid contains 459 million tetrahedral cells but only 78 million nodes. Hence, the USM3D solutions have approximately six times as many degrees of freedom as FUN3D solutions on the same grid, and the representative cell size for the wake gridding would be twice as large in the FUN3D solution as in the USM3D solution. Consequently, to obtain a direct comparison between the USM3D and FUN3D solvers, a much finer grid must be generated for the FUN3D solution. However, the grid generation code VGRID was unable to successfully generate the volume grid for grids much larger than the medium grids generated for USM3D. Therefore, the VGRID process was pushed to the limit, and the largest grid that was created had 717 million cells and 122 million nodes, such that the number of degrees of freedom (DoF) in the following FUN3D solutions was about 26% of the DoF in the USM3D solutions.

Simulations on the SLS Block 1 Crew configuration were conducted with FUN3D version 12.7. Modeling options were thoroughly exercised with runs conducted at $\alpha_P = 30$ and 90 deg and $\phi_P = 0$ deg. Simulations for RANS, DDES, and MDDES used the standard SA model, SA with a rotation correction (results not included in this paper for brevity), and SA with both rotation and curvature corrections (SA-RC). Solutions with the incompressible formulation were only made with the RANS and DES methods using standard SA. The solutions were run at a normalized time step of $\Delta t = 50$ for 2,000 time steps; then $\Delta t = 25$ for 2000 time steps; then, if a statistical steady state was reached, another 4000 time steps for the time-averaging window. As with USM3D, 10 subiterations per time step were used with FUN3D. For the SLS Block 1 Crew cases, a statistically steady state was reached at anywhere from 4000 to 8000 time steps, with the $\alpha_P = 90$ deg cases taking the longest to reach that state.

One of the more interesting findings from the FUN3D results was the sensitivity of the Coanda state to the DES method and turbulence model. The effect of model on Coanda state is demonstrated in Fig. 13, in which the instantaneous M contours at station 4 for the DDES SA, DDES SA-RC, and MDDES SA compressible runs for one condition are shown at $\alpha_P = 90$ deg and $\phi_P = 0$ deg; green contours denote the windward freestream flow on the bottom of the figure, blue denotes low-speed flow, and red denotes high-speed flow. It is clearly evident that with DDES SA the flow through the gaps attached to the port SRB and starboard side of the centerbody. However, the gap flow attached to both sides of the centerbody with DDES SA-RC and attached to both of the SRBs with MDDES SA. The results at this one condition suggest that the Coanda state that will be expressed is very sensitive to the computational setup. This has been confirmed with other runs in which changes in the time step and in the resolution of the unstructured grid have yielded a change in the Coanda state. Moreover, validation of the computational setup against experimental data is quite tricky, as the CFD simulation may have captured a different Coanda state than the experimental run, and the repeatability of the experimental runs themselves is uncertain.

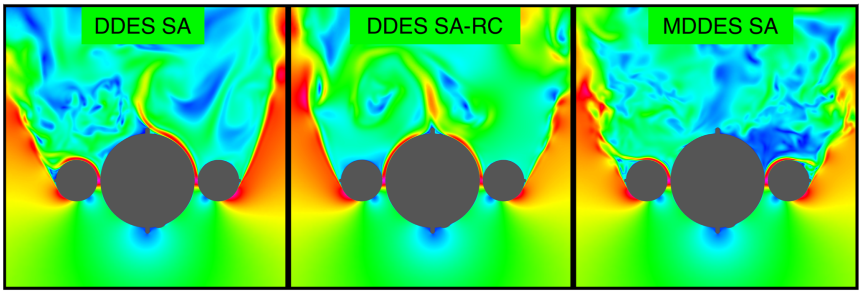

Fig. 13 Instantaneous Mach Contours at station 4 for FUN3D using DDES SA, DDES SA-RC, and MDDES SA for the SLS Block 1 Crew configuration at $M = 0.183$, $\alpha_P = 90$ deg and $\phi_P = 0$ deg.

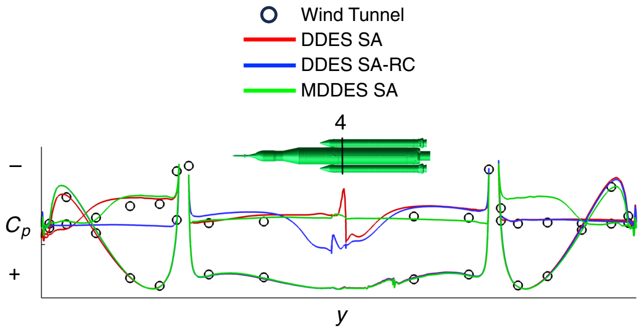

Fig. 14 Effect of FUN3D DES method and turbulence model on C_p and comparison to wind-tunnel data for station 4 for the SLS Block 1 Crew configuration at $M = 0.183$, $\alpha_P = 90$ deg, and $\phi_P = 0$ deg.

Corresponding plots of the pressure coefficient data for the wind tunnel and the three simulations are shown in Fig. 14. For each of the cases, the most negative pressures on the leeward surfaces were associated with the corresponding flow through the gap that wrapped around and attached to a given component. Even though the DDES SA result exhibited the best correlation with the wind-tunnel values, because it captured the same Coanda state as observed in the wind tunnel, the other solutions were still valid, as even small changes in geometry or conditions may trip the Coanda effect into a different state.

Similarly to the issue with the Coanda state, the simulations at $\alpha_P = 30$ deg were difficult to assess because the correlation with experiment was dependent on whether or not the method captured the orientation of the asymmetric vortices expressed in the wind tunnel. Altogether, FUN3D simulations from 14 different combinations of turbulence model and flow solver model were completed and all had reasonably similar results. Again, with little to distinguish the results in a meaningful way, the most straightforward conclusion was to select the compressible DDES SA method for use in grid and time step resolution studies. Of course, due to the sensitivity of the phenomena, refinements in both grid resolution and time step frequently flipped the orientation of either the asymmetric vortices, the Coanda state, or both.

C. Evaluation of Kestrel

The Kestrel dual mesh approach provided a significant advantage in simulating flows that contained regions of massively separated flow. In these cases, the extensive wake on the leeward side of the body were resolved in the off-body Cartesian mesh, for which operations were significantly cheaper to implement than operations on the near-body unstructured grid. Moreover, the Cartesian mesh was much more suitable for the use of higher-order spatial discretization and was amenable to the implementation of AMR. Finally, the AMR in the dual mesh approach provided the opportunity to achieve the greatest possible accuracy while running on the smallest possible grid. Note that the dual mesh AMR approach required verification studies like domain extent, refinement threshold value and parameter, refinement frequency, and overlap distance.

The flow solver within Kestrel that was employed on the near-body domain was KCFD, a cell-centered, finite volume method for solving the Euler and RANS equations on mixed-element unstructured meshes. Available turbulence models included a number of the SA variants and the Menter two-equation model with and without shear stress transport. In addition to the traditional RANS capability, KCFD provided an option for DDES at the time of this work, for use in situations involving massively separated flow. The CFD code employed on the off-body domain was SAMAir, a finite difference method for solving the Euler and RANS equations on Cartesian meshes that was derived from an earlier code, ARC3DC, developed at the NASA Ames Research Center. SAMAir was capable of implementing all the models available in KCFD, allowing for a uniform implementation of the governing equations in both solvers.

While there were numerous Kestrel input parameters to be set for LOT simulations, the LaRC SLS CFD team was fortunate enough to have the initial input parameters set up by the lead authors of Ref. [17]. Consequently, most of the effort in exploring options for the Kestrel input parameters were in regard to the resolution and extent of the solution adaption region for the wake. The Kestrel input parameters were verified and updated after this work and are discussed in Ref. [4].

To illustrate some of the mesh details, the instantaneous vorticity at a cross-section of station 5, for a Kestrel grid generated at the end of a simulation for the Block 1 configuration at $M = 0.183$, $\alpha_P = 30$ deg, and $\phi_P = 0$ deg, is shown in Fig. 15. In the main portion of the figure, the unstructured grid around the vehicle was not shown in order to clearly delineate the extent of the Cartesian grid in the vicinity of the body; the offset figure shows the overlap between the unstructured grid and the Cartesian mesh in the gap between the port SRB and the centerbody. The position of the overlap region was dictated by the trim distance used in trimming down the unstructured grid and the size of the grid cells at the outer edge of the unstructured grid; in this case, the trim distance is 24 in. The overset mesh is a nonconservative region between the near-body and off-body grids, and the trim distance was later evaluated and moved farther away from the vehicle surface and the associated flow effects.

The near-body unstructured grid for the Kestrel simulations was very similar to that for USM3D, as the only difference in generating the grids was with regard to the volume sources. For USM3D, the volume sources for capturing the wake needed to be manually skewed and aligned with the freestream flow direction for each roll angle; otherwise, a large cost would be paid for refining the region upstream of the vehicle where nothing of interest was happening. In contrast, the Kestrel unstructured grid was trimmed to form the near-body grid only, so it was not that costly to refine upstream of the vehicle. Hence, for the Kestrel grids, the volume sources for the centerbody and SRBs were centered on the centerline of the respective component, and one grid suffices for all roll angles. Upon generation of the grid, the Carpenter Grid Utility released with Kestrel was used to trim the near-body grid and merge the tetrahedral elements into mixed elements, such as prisms and pyramids. The resulting near-body grid was approximately 100 million cells. In comparison, over development of the solution, the size of the off-body Cartesian grid grew from around 300 million points and leveled out at about 1.1 billion points.

The spatial extent of the Cartesian grid solution refinement was specified in the input file as approximately twice the nominal centerbody diameter from the centerline, in both directions along the y and z axes. The Cartesian grid only gets refined in regions where the value of a specified flowfield variable exceeded a specified threshold. For the SLS LOT solutions, adaptive mesh refinement was based on the magnitude of the vorticity, with a threshold set at 100/s; this threshold value corresponded to the yellow contours in the Fig. 15. No grid refinement occurred upstream of the vehicle or other areas where the vorticity magnitude was zero. Extensive refinement occurred on the leeward side of the vehicle, but even there, the adaption method was

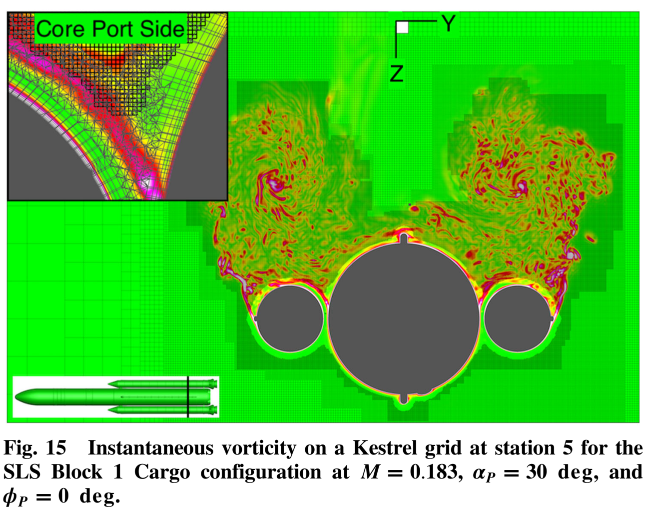

Fig. 15 Instantaneous vorticity on a Kestrel grid at station 5 for the SLS Block 1 Cargo configuration at $M = 0.183$, $\alpha_P = 30$ deg, and $\phi_P = 0$ deg.

efficient, as there was little refinement behind the center of the centerbody.

Simulations on the SLS Block 1 Crew configuration were conducted with Kestrel version 7.1.2. For both the KCFD and SAMAir codes, simulations were conducted with the DDES approach and the SA turbulence model, inviscid fluxes were discretized with the HLLE++ method, convective fluxes were handled with the Van Leer flux splitting scheme, and the second-order temporal discretization was handled with Gauss–Seidel. The most significant differences between inputs for the two Kestrel flow solvers were that the spatial discretization was second order and the temporal advective damping was set to 0.01 for KCFD, whereas for SAMAir the spatial discretization was third order and the temporal advective damping was set to 0.02. The dimensional time step was set at $dt = 0.0005$ s with three subiterations per time step and a maximum of 32 sweeps per subiteration. The AMR was performed every 250 time steps. The nominal procedure was to run a simulation for 10,000 time steps, and then continue for another 4000 time steps with the time-averaging procedure. However, the time-averaging procedure was occasionally initiated earlier than that if the solution appeared to reach a statistical steady state sooner, or restarted at 14,000 time steps and run another 4000 times steps with time averaging if the solution required more iterations.

D. Comparison of USM3D, FUN3D, and Kestrel

The relative suitability of the three codes for simulations of the SLS LOT phase of flight was assessed by comparing results for a pitch sweep at $\phi_P = 0$ deg. While the correlations between the numerical and wind data were crucial, the computational expense of the runs was just as influential in the selection of the tool for constructing the databases.

The trends seen in comparing results from different formulations of a single solver, where any change in parameters, CFD models, or grids was likely to cause a change in the orientation of the asymmetric vortices and/or the Coanda state, was also experienced in comparing the selected models for each code against each other. For instance, the comparison of C_p between the wind tunnel and CFD data, at station 4 on the SLS Block 1 Crew configuration at $\alpha_P = 90$ deg and $\phi_P = 0$ deg, provided evidence that the solutions captured different Coanda states (Fig. 16). The flow through the gaps attached to both sides of the centerbody for Kestrel, attached to the port SRB and starboard side of the centerbody for FUN3D and the wind-tunnel environment, and attached to both of the SRBs for USM3D. The FUN3D model also caught the same orientation of the asymmetric vortices at $\alpha_P = 30$ deg and $\alpha_P = 50$ deg as was experienced in the wind tunnel, whereas the Kestrel and USM3D models caught the opposite orientation. Note, however, that whether or not a particular simulation captured the wind-tunnel environment asymmetric vortex or Coanda state was not considered as a code selection criterion because the phenomena were so sensitive to small perturbations in the wind-tunnel environment and to the CFD parameters.

In terms of the correlation of the force and moment coefficients between the three codes and the wind-tunnel database, the predictions from all three codes were deemed to be sufficient. For normal force, which was the dominant force along the $\phi_P = 0$ deg pitch sweep, the CFD predictions were within approximately 4% of each other and were within the uncertainty band of the wind tunnel. All the CFD codes underpredicted side force relative to the wind-tunnel data, with the USM3D and Kestrel in good agreement as they were within 5% of each other. The FUN3D side force prediction was an outlier, but keep in mind that a much finer grid would be required for FUN3D to be of a comparable resolution to the USM3D and Kestrel meshes.

The resource requirements for the three CFD flow solvers using the baseline settings, along with a few variants, conformed to expectations and are shown in Table 1. The times listed represent the time required to reach a statistical steady state and run an appropriate number of additional time-averaging iterations for simulations of the SLS Block 1 Crew at LOT conditions using 1200 Haswell processors on the NAS Pleiades cluster. Note that the number of unknowns was proportional to the number of cells for USM3D, the number of nodes for FUN3D, and both the number of nodes (Cartesian grid) and cells (unstructured grid) for Kestrel. The initial USM3D runs were quite slow, even with the improved time marching procedure. The fastest of the USM3D runs took the same amount of time as the slowest of the FUN3D runs. However, taking into consideration that a finer grid was required for FUN3D to have the equivalent DoF to that of USM3D to that of USM3D, then the USM3D and FUN3D computational resource requirements would likely be fairly equivalent. Although it was expected that the incompressible FUN3D model would be faster than the equivalent compressible model, it was quite surprising that runs on the mixed element mesh took 40% more time than runs on the tetrahedral mesh. The Kestrel code (version 7.1.2 on NAS) delivered solutions two to four times faster than the USM3D code with the improved time stepping procedure. Furthermore, the same problem using Kestrel version 8 on a DOD Eglin cluster gained another factor of 2 improvement in speed.

The focus of the study was to determine which code could produce a large database of CFD runs with minimum resources and acceptable accuracy. Because comparisons of the CFD results with wind-tunnel data were reasonable, and the discrepancies could be reasoned to be present from asymmetric vortex or Coanda state variations, any of the codes could have been selected for database production runs. The deciding factor was the speed at which solutions could be computed, which provided a clear selection among the three codes investigated.

Considering the massive size of the required grids, Kestrel provided a significant reduction in the time needed for the overall CFD workflow. Unlike the detailed gridding requirements for USM3D and FUN3D, the same near-body grid was used for every Kestrel solution, obviating the need for unique unstructured grids for each roll condition. Though FUN3D does have built-in AMR capability, the refinement is performed on an unstructured mesh, making it substantially less computationally efficient than adaption on a Cartesian grid, as employed in Kestrel. Consequently, based on grid and solution efficiency, Kestrel was the clear choice as the tool to use for future LOT simulations.

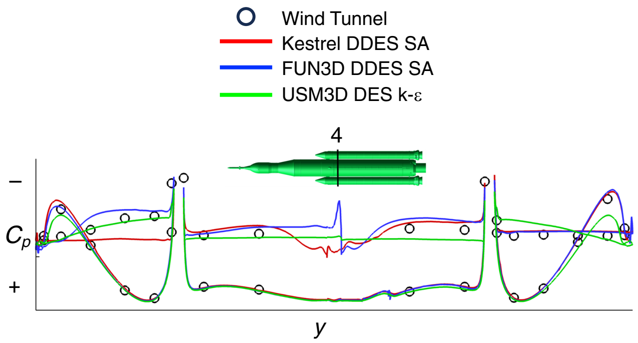

Fig. 16 Effect of CFD code and turbulence model on C_p and comparison to wind-tunnel data for station 4 on the SLS Block 1 Crew configuration at $M = 0.183$, $\alpha_P = 90$ deg, and $\phi_P = 0$ deg.

IV. SLS Block 1B Crew and Cargo (2016–2018)

Based on the lessons learned on the Block 1 Crew configuration, analyses of the Block 1B Crew and Cargo configurations proceeded with Kestrel as the flow solver, running DDES with the SA turbulence model and AMR based on a vorticity magnitude threshold of 100/s. The runs for both Block 1B configurations were conducted with version 7.1.2 of Kestrel.

The Block 1B Crew configuration for analysis involved a more detailed geometry with the addition of numerous protuberances, relative to the DAC2 Block 1 Crew configuration. The CFD OML for the Block 1B Crew configuration is shown in Fig. 17. The most significant differences were the 11 additional rings on each of the SRBs; four additional rings at the top of the centerbody; and significantly more detail in the representations of the attach brackets, feedlines, and system tunnels. It should be noted that the locations of the first two pressure port rings were different from one configuration to

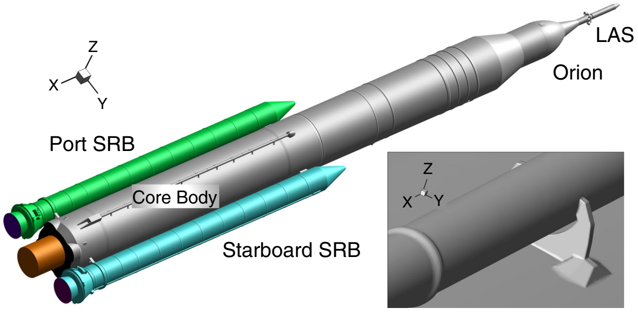

Fig. 17 The CFD OML for the Block 1B Crew configuration. The inset image on the right depicts the feedline with bracket.

another, as they have different geometries forward of the common centerbody.

An indication of how meticulous the expectation for CFD modeling has become can be gleaned from the bottom-right inset of Fig. 17, which highlights the detail with which the feedline brackets were represented. Given that there were nine brackets on each of the two feed lines, the increase in grid size due to modeling of the brackets was substantial; unfortunately, there was neither the time nor resources to make and run an additional CFD case without the brackets to see if the influence of the brackets could be quantified. Upon merging tetrahedra into prisms to create a mixed-element grid, then trimming the grid to 24 in., the size of the SLS Block 1B Crew near-body unstructured grid was approximately 120 million cells.

The initial CFD model for the Block 1B Cargo configuration was quite similar to that for the crew configuration, as the lower two-thirds of the cargo OML was identical to that of the crew OML. The only difference between the crew and cargo configurations was the Orion/LAS and the cargo payload fairing portions of the geometry.

A significant change was also made in the wind-tunnel methodology between Test 609 for the Block 1 vehicle and Test 633 for the Block 1B vehicles. In Test 633, the decision was made to gain component-level force and moment breakdowns at the cost of pressure information on the SRBs. By installing load cells in both the forward and aft attach brackets for the SRBs, forces and moments on the centerbody and the two SRBs could be distinguished. However, the installation precluded the ability to instrument the pressure ports on the SRBs, so it was no longer possible to discern how well CFD pressure distributions on the SRBs correlated with wind-tunnel pressure port values.

A. Kestrel Results for SLS Block 1B Crew (2016–2017)

The decision was made to producee one-quadrant ROM from CFD simulations executed betweeen $\phi_P = 0$ and 90 deg for the SLS Block 1B Crew database because of the long wait times that were experienced in the Pleaides queue at NAS. The single-quadrant ROM was then reflected in roll angle to the other three quadrants, then anchored to the wind-tunnel force and moment database in all four quadrants to yield the final DFROM. Refinements in selecting the run matrix were also made in an effort to improve upon the equally spaced matrix used for the Block 1 configuration. This involved running RANS simulations at $\alpha_P = 15$ deg rather than $\alpha_P = 10$ deg and then using a DoE approach to optimize the placement of points for running DDES simulations at total angles of attack greater than 20 deg. The DoE relied on the Block 1 results and wind-tunnel data from Block 1B and focused on maximizing a performance function that sought to achieve CFD force and moment results as close to measured wind-tunnel data as possible. The final optimized matrix is shown in Fig. 18.

Although RANS solutions were deemed to be sufficient for $\alpha_P <$ 15 deg, the initial results from the simulations at $\alpha_P = 15$ deg did not correlate well with the experimental data, particularly in regard to the leeward surface pressures on the centerbody. To resolve the discrepancy, the DDES and AMR modeling that was used at $\alpha_P > 15$ deg was also used at $\alpha_P = 15$ deg, but on the RANS grid rather than the DDES grid, with the AMR limited to three levels of grid refinement. This hybrid method resulted in solutions that were much better correlated with wind-tunnel data at little cost, as the Cartesian mesh grew from an initial 120 million points to around 190 million points.

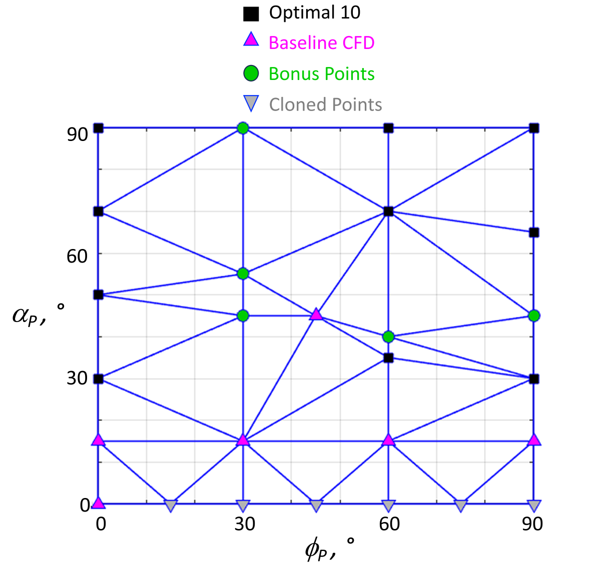

Fig. 18 Optimal distribution of CFD points from the DoE for $\alpha_P > 15$ deg.

Other than the need to use different grids at lower angles of attack, completion of the SLS Block 1B Crew run matrix proceeded smoothly. The AMR was well behaved; the Cartesian mesh grew from about 300 million points to 1.2 billion points at $\alpha_P = 30$ deg and up to 2 billion points at $\alpha_P = 90$ deg. A sample of the force and moment coefficients are shown in Fig. 19, for a pitch sweep at $\phi_P = 0$ deg. The agreement between the wind-tunnel database and Kestrel CFD for the normal and side force is very good and agree moderately well for the pitching and yawing moments.

It should be noted that the magnitudes of the rolling moment coefficient were very small, as the alpha sweep shown is at zero roll angle. Further, at very high angles of attack (near $\alpha_P = 90$ deg), the axial force coefficient was of little consequence. The trend in the wind-tunnel side force coefficients indicates that the orientation of the asymmetric vortices flipped from one state to the other between $\alpha_P = 20$ deg and $\alpha_P = 25$ deg, flipped again between $\alpha_P =$ 30 deg and $\alpha_P = 35$ deg, and then flipped again after $\alpha_P =$ 40 deg as evident by the sign change in C_Y. The most puzzling point was at $\alpha_P = 30$ deg, for which the computed yawing moment coefficient substantially underpredicted the wind-tunnel data, and yet the side force comparison was quite well aligned.

Overall, the computed results for the SLS Block 1B Crew configuration were well behaved, agreed well with experiment, and used about a quarter of the resources used in simulations for the SLS Block 1 Crew database. These metrics represented significant advances in the team's tools, processes, and workflow.

B. Kestrel Results for SLS Block 1B Cargo (2017–2018)

The development of the transition database for the Block 1B Cargo configuration followed the same workflow and process as for the SLS Block 1B Crew configuration. The mixed element unstructured grid, trimmed to 24 in., contained 112 million cells. No changes were made to the DOE matrix, based on comparison of available data.

Although initial CFD simulations were being incorporated into the ROM, the CFD solutions near $\alpha_P = 70$ deg exhibited side force coefficients well beyond what was observed in the force and moment database. The source of the discrepancy in the side force was isolated to a region downstream of the cargo fairing and upstream of the SRBs through the comparison of surface pressure coefficients between wind-tunnel and CFD data. The Kestrel surface pressure coefficient distribution on the leeward side of the vehicle at $M = 0.183$,

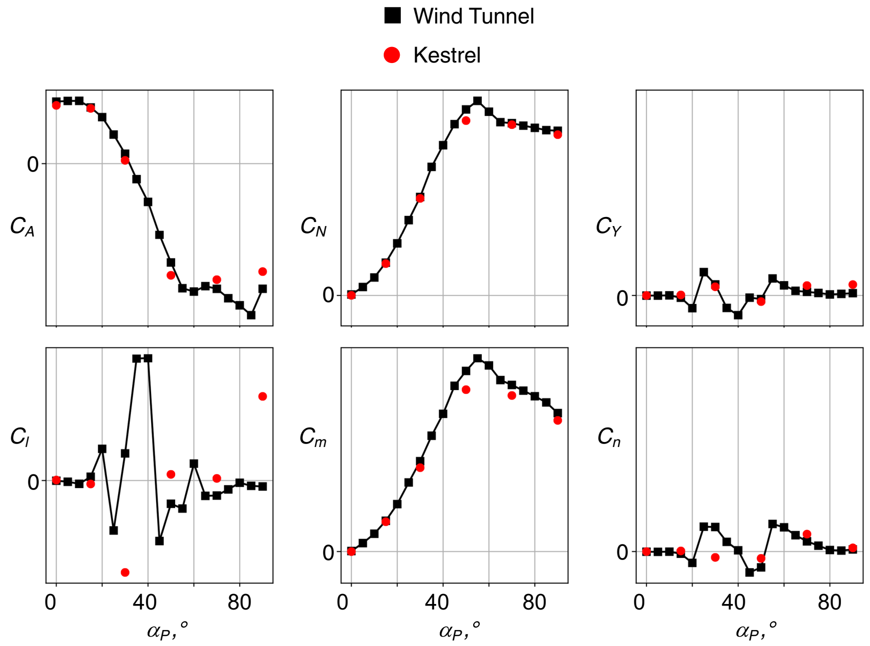

Fig. 19 Coefficient comparisons between wind-tunnel and Kestrel data for the SLS Block 1B Crew configuration at $M = 0.183$ for a pitch sweep at $\phi_P = 0$ deg.

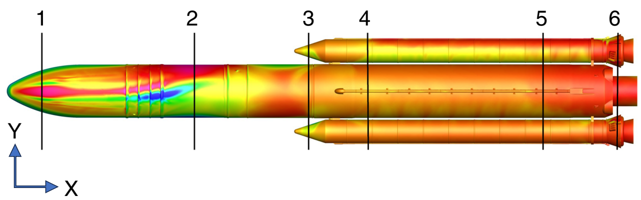

Fig. 20 Stations 1–6 and Kestrel DDES SA C_p data on the leeward surface of the SLS Block 1B Cargo configuration at $M = 0.183$, $\alpha_P = 70$ deg, and $\phi_P = 0$ deg.

$\alpha_P = 70$ deg, and $\phi_P = 0$ deg is shown in Fig. 20 for the solution with a grid trim distance of 24 in. As will be shown the comparison of the computational and wind-tunnel pressure coefficients were in good agreement at station 1, but the simulation was grossly inaccurate on the leeward side of the vehicle at station 2. This comparison allowed the team to isolate the source of the discrepancy to the area forward of station 2.

Initially, the source of the problem was hypothesized to lie in the gridding of the four rings and protuberances ahead of station 2; however, the grid at these locations appeared satisfactory, and the discrepancies persisted even after mesh refinement of the protuberances. For further investigation of the anomaly, the team simplified the problem by truncating all geometry aft of the SRB noses from the computational model, but the anomaly was not recreated in this case, nor when just the SRBs and attach brackets were removed from the model. However, when the attach brackets and noses of the SRBs were reintroduced to the truncated model, the anomaly reappeared. A solution to the problem was found by investigating larger near-body trim distances on this modified truncated geometry.

The original unstructured grid for the SLS Block 1B Crew configuration was refined around the four rings and the protuberances in the vicinity of the rings, then trimmed, and simulations were conducted. A plot of the centerbody side force coefficient sectional lineloads for each of the grid trim values is shown in Fig. 21, in which wld7 refers to the baseline mesh refinement level on the protuberances and wld8 refers to the improved mesh refinement on the protuberances. The magnitude of the asymmetry for the 30 and 36 in. trim cases was much less than that of the asymmetry captured in the lower trim cases, and the directionality of the vortex pair had switched. Both of these results were more in line with what was observed in wind-tunnel testing.

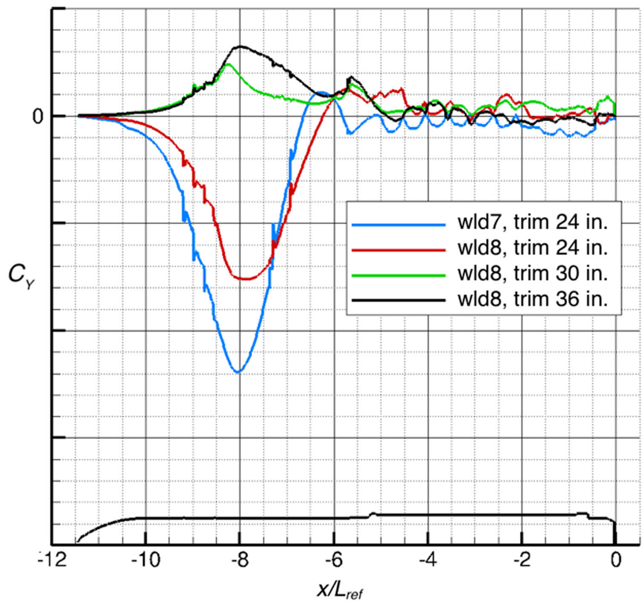

Fig. 21 Effect of grid refinement and trim distance on the centerbody sectional side force coefficient lineloads for the SLS Block 1B Cargo configuration at $\alpha_P = 70$ deg and $\phi_P = 0$ deg.

The pressure coefficients for the simulations with trim distances at 24, 30, and 36 in. are shown at the first three stations for the $\alpha_P = 70$ deg, $\phi_P = 0$ deg case in Fig. 22. It is evident that for the grid trimmed to 24 in the computed values were in good agreement with wind-tunnel values over the centerbody at station 1 but were wildly inaccurate at stations 2 and 3, where the expansion was overpredicted on the leeward side of the vehicle. For the trim distances at 30 and 36 in., the results at stations 2 and 3 were in good agreement with each other and in fairly good agreement with the wind-tunnel results.

Either the 30 or 36 in. trim distance could have been chosen for completion of the simulations on the SLS Block 1B Cargo configuration because the results were similar. Although the choice of the 30 in. trim distance required lower use of computational resources, the 36 in. trim distance was chosen for additional margin, as it moved the nonconservative overset mesh region between the near-body and

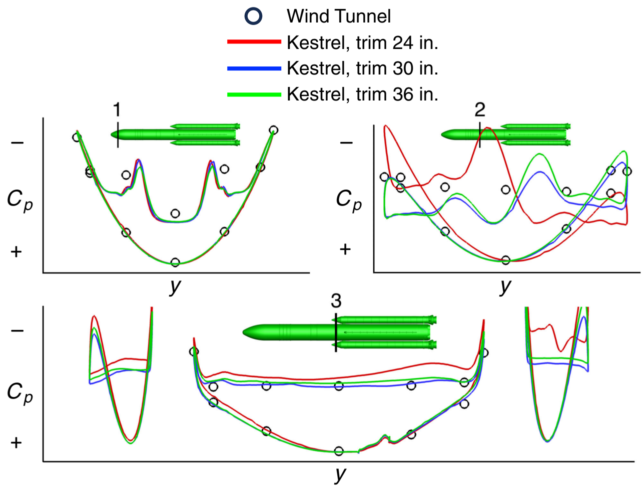

Fig. 22 Effect of Kestrel trim distance on C_p and comparison to wind-tunnel data for the SLS Block 1B Cargo configuration at $M = 0.183$, $\alpha_P = 70$ deg, and $\phi_P = 0$ deg.

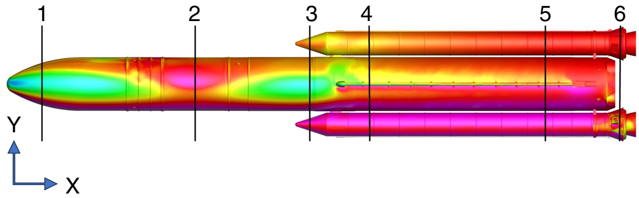

Fig. 24 Stations 1–6 and pressure contours from Kestrel DDES SA on the SLS Block 1B Cargo configuration at $M = 0.183$, $\alpha_P = 70$ deg, and $\phi_P = 270$ deg.

off-body grids, farther away from the vehicle surface and associated flow effects.

The thoroughly peculiar behavior observed in the simplified problems that were tested, namely, that the issue did not arise until the noses of the SRBs were included in the simplified model, led to an in-depth investigation into all the output parameters from the solutions and a lot of the input parameters to the code. Nothing of note was discovered; the residuals for each time step converged nicely; force and moment histories were normal; bizarre flow features could not be extracted. Eventually, it was conjectured that the result of the interaction effects in the overlap region between the unstructured and Cartesian grids in the region of the SRB noses, particularly in the gap between the centerbody and noses, caused the problem; the logic behind that supposition is that with a trim distance too small to close the gap between the components with the unstructured grid alone regions of the flow were interpolating data from the outer layers of the unstructured grids for the centerbody and the SRBs and from the Cartesian grid. The chances of the scheme preserving conservation of mass and momentum in this region seems dubious at best.

Even after problems with the cases at $\alpha_P = 70$ deg were addressed through the increase of the near-body grid trim distance to 36 in., additional difficulties were encountered in the development of an appropriate DFROM for the SLS Block 1B Cargo database. The trouble arose from the number of cases for which the CFD solutions captured the asymmetric vortices of the opposite orientation than what was observed in the wind tunnel. This led to problems in anchoring the ROM to the wind-tunnel database force and moment values, as the DFROM yielded lineloads that were implausible.

In response to these challenges, the team expanded the CFD matrix to cover all four quadrants and generated the missing lineloads data. This eliminated the need to rotate and reflect solutions, which reduced the number of multiple core solutions delivered from 4 to 2. Further, the decision was made to unconstrain the DFROM from having to match all wind-tunnel nominal force and moment coefficients and restrict the matching to normal force and pitching moment coefficients. This change resulted in much more physically realistic lineloads as well as a closer match to wind-tunnel force and moment coefficients. The maturation of the tools, processes, and workflow allowed the expansion of the CFD matrix for the Block 1B Cargo vehicle from 21 points in a single quadrant of roll angle to 65 points spanning all four quadrants of roll angle for a higher-quality database. The difference in data source for each breakpoint is shown graphically in Fig. 23.

Unfortunately, a new anomaly in the CFD solutions arose while running CFD in all four quadrants of roll. Once again, the problem that arose at $\alpha_P = 70$ deg and $\phi_P = 0$ deg was also evident at $\phi_P = 270$ deg. The surface pressure coefficient distribution on the upper side of the vehicle at $\alpha_P = 70$ deg and $\phi_P = 270$ deg is shown in Fig. 24; the flow direction is from the bottom of the figure to the top.

A comparison of the CFD-computed and wind-tunnel-measured surface pressure coefficients for a flow condition near where the maximum body-axis side force loading was observed in the wind-tunnel force and moment database is shown in Fig. 25 for the foremost three stations. Once again, the problem occurs at or near station 2, propagating downstream to station 3. This provided a strong indication that the change in trim distance did not address the fundamental weakness of the gridding strategy. The issue was revisited for the analysis cycles that followed this work.

The subsequent analysis cycles used the unstructured grid generation software by Helden Aerospace, Inc. [24], instead of GTC and VGRID. Preliminary studies showed that HeldenMesh addressed the gridding deficiencies that had been difficult to overcome using the present set of tools. The significantly decreased turnaround time to

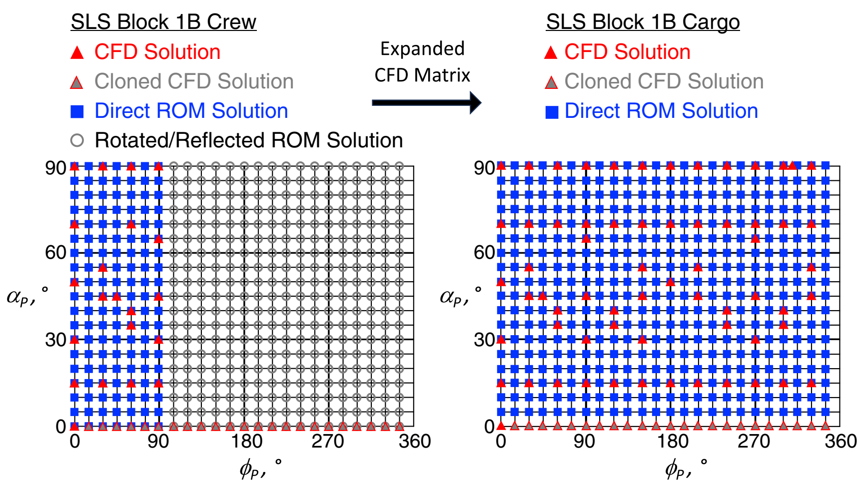

Fig. 23 Effect of expanding CFD capability on delivered databases between the Block 1B Crew and Cargo analysis cycles.

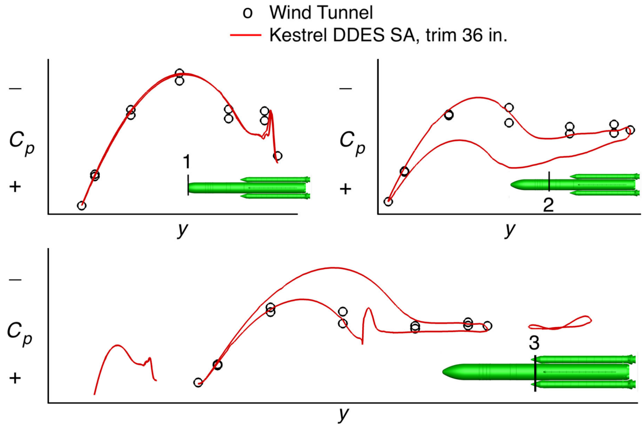

Fig. 25 Comparison of C_p between wind-tunnel and Kestrel DDES SA data for the SLS Block 1B Cargo configuration at $M = 0.183$, $\alpha_P = 70$ deg, and $\phi_P = 270$ deg.

generate new grids with HeldenPatch and HeldenMesh should enable more rigorous grid studies than previously possible, and results of these studies were anticipated to yield further understanding of the impact of the gridding approach on the flowfield solutions for the SLS liftoff and transition problem.

V. Conclusions

This report documents some of the reasoning and decisions related to the selection of tools for the liftoff and transition phase of flight of the Space Launch System launch vehicle, along with the evolution of the approach over the course of analyzing multiple SLS configurations. Upon the evaluation of three state-of-the-art computational fluid dynamics flow solvers, the Kestrel flow solver was selected for use in developing the LOT lineloads databases. Although all three flow solvers generally predict similar results, the selection of Kestrel was due primarily to the significant savings in the CFD solution development turnaround time relative to the workflows for USM3D and FUN3D. The reduction in solution time outweighed the additional time needed to acquire and vet the Kestrel solver. Although FUN3D and USM3D do have limited means of adapting the mesh based on the flow using accompanying tools, the built-in, off-body, Cartesian automatic mesh refinement capability in Kestrel was found to be far superior in terms of both usability and computational efficiency. The real power of Kestrel was the combination of AMR and delayed detached eddy simulation that was not available with FUN3D or USM3D at the time of this work. The FUN3D flow solver has since added AMR with unsteady schemes.

A turbulence model study showed that the one-equation SA model performed as well as the more computationally expensive two-equation k-ϵ and SST models for this problem. The DDES approach provided more accurate (closer to wind tunnel) results than RANS, which was expected due to the presence of the large leeward trailing-wake flowfield at such high angles of attack. Thus, the SA model with DDES was chosen for the LOT simulations at higher angles of attack, where massive separation dominated the character of the leeward flow, with the RANS approach used only for cases at a total angle of attack of 15 deg or less.

A grid trim value of 24 in. was used on the SLS Block 1 and 1B Crew configurations. Grid trim distance studies during the analysis of the Block 1B Cargo configuration showed that significant changes occurred in nominal force coefficients between trim values of 24 and 36 in. but that vortex asymmetry remained generally consistent for trim values between 30 and 36 in. A grid trim value of 36 in. was thus deemed appropriate for the LOT work on the SLS Block 1B Cargo configuration.

Each configuration and analysis cycle brought with it new challenges, but the team steadily improved computational tools, processes, workflow, and understanding of the aerodynamic complexities unique to the LOT flow regime. The follow-up work included efforts toward a rigorous verification of the improved DDES approach for the LOT problem. Additionally, new tools and approaches for gridding were explored to address many of the gridding shortcomings identified in this paper.

References

[1] "NASA: SLS Evolvability, Foundation for a Generation of Deep Space Exploration," Aug. 2020, https://www.nasa.gov/image-article/sls-block-1-crew-block-1b-crew-block-1b-cargo-block-2-cargo-evolution/ [retrieved 29 May 2024].

[2] Sohail, M., Chao, Y., Ullah, R., and Yamin, M., "Computational Challenges in High Angle of Attack Flow," *World Academy of Science, Engineering and Technology*, Vol. 80, No. 1, 2011, pp. 1148–1155.

[3] Fidler, J., and Bateman, M., "Asymmetric Vortex Effects on Missile Configurations," *Journal of Spacecraft and Rockets*, Vol. 12, No. 11, 1975, pp. 674–681.
https://doi.org/10.2514/3.57034

[4] Pomeroy, B. W., and Krist, S. E., "Validation of Kestrel IDDES Simulations for SLS Transition Analysis," AIAA Paper 2022-1335, 2022.
https://doi.org/10.2514/6.2022-1335

[5] Pomeroy, B. W., Krist, S. E., Wignall, T. J., Deere, K. A., Lee, M. W., Ghaffari, F., Collins, J. G., Ratnayake, N. A., Streett, C. L., Goushcha, O. O., et al., "An Overview of NASA Langley Low-Speed CFD Contributions to the Space Launch System Program," AIAA Paper 2023-0236, 2023.
https://doi.org/10.2514/6.2023-0236

[6] Chan, D. T., Paulson, J. W., Shea, P. R., Toro, K. G., Parker, P. A., and Commo, S. A., "Aerodynamic Characterization and Improved Testing Methods for the Space Launch System Liftoff and Transition Environment," AIAA Paper 2019-3398, 2019.
https://doi.org/10.2514/6.2019-3398

[7] Walker, M. A., Pinier, J. T., Shea, P. R., Collins, J. G., Mears, L. J., Lee, M. W., and Pomeroy, B. W., "Experimental Identification of Bistable Flow States on the Space Launch System at Liftoff Conditions," AIAA Paper 2022-3665, 2022.
https://doi.org/10.2514/6.2022-3665

[8] Hartwich, P., Hall, R., and Hemsch, M., "Navier-Stokes Computations of Vortex Asymmetries Controlled by Small Surface Imperfections," AIAA Paper 1990-0395, 1990.
https://doi.org/10.2514/6.1990-385

[9] Levinsky, E. S., and Yeh, T. T., "An Analytical and Experimental Investigation of Circulation Control by Means of a Turbulent Coanda Jet," NASA CR-2114, 1995.

[10] Capone, F. J., Paulson, J. W., Jr., and Erickson, G. E., "Liftoff and Transition Aerodynamics of the Ares I (A106) Launch Vehicle," AIAA 2011-0997, 2011.
https://doi.org/10.2514/6.2011-997

[11] Krist, S. E., Ratnayake, N. A., and Ghaffari, F., "Kestrel Results at Liftoff Conditions for a Space Launch System Configuration in Proximity to the Launch Tower," *AIAA Aviation Forum*, AIAA Paper 2019-3400, 2019.
https://doi.org/10.2514/6.2019-3400

[12] Strelets, M., "Detached Eddy Simulation of Massively Separated Flows," AIAA Paper 2001-0879, 2001.
https://doi.org/10.2514/6.2001-879

[13] Spalart, P., Deck, S., Shur, M., Squires, K., Strelets, M. K., and Tavin, A., "A New Version of Detached-Eddy Simulation, Resistant to Ambiguous Grid Densities," *Theoretical Computational Fluid Dynamics*, Vol. 20, July 2006, pp. 181–195.

[14] Spalart, P. R., "Comments on the Feasibility of LES for Wings, and on a Hybrid RANS/LES Approach," *Proceedings of 1st AFOSR International Conference on DNS/LES*, Greyden Press, 1997.

[15] Frink, N. T., Pirzadeh, S. Z., Parikh, P. C., Pandya, M. J., and Bhat, M., "The NASA Tetrahedral Unstructured Software System(TetrUSS)," *Aeronautical Journal*, Vol. 104, No. 1040, 2000, pp. 491–499.
https://doi.org/10.1017/S0001924000091995

[16] Biedron, R. T., Carlson, J.-R., Derlaga, J. M., Gnoffo, P. A., Hammond, D. P., Jones, W. T., Kleb, B., Lee-Rausch, E. M., Nielsen, E. J., Park, M. A., et al., "FUN3D Manual: 13.2," NASA TM-2017-219661, 2017.

[17] Morton, S. A., McDaniel, D. R., Sears, D. R., Tillman, B., and Tuckey, T. R., "Kestrel - A Fixed Wing Virtual Aircraft Product of the CREATE Program," AIAA Paper 2009-0338, 2009.
https://doi.org/10.2514/6.2009-338

[18] Bozeman, M. D., "TetrUSS: Tetrahedral Unstructured Software System, Publications," NASA Langley Research Center, https://tetruss.larc.nasa.gov/tetruss-related-publications/ [retrieved June 2023].

[19] Wignall, T. J., "Liftoff and Transition Database Generation for Launch Vehicles Using Data-Fusion-Based Modeling," AIAA Paper 2019-3401, 2019.
https://doi.org/10.2514/6.2019-3401

[20] Abdol-Hamid, K. S., Ghaffari, F., and Parlette, E., "Overview of Ares-I CFD Ascent Aerodynamic Data Development and Analysis Based on USM3D," AIAA Paper 2011-0015, 2011.
https://doi.org/10.2514/6.2011-15

[21] Abdol-Hamid, K. S., Ghaffari, F., and Parlette, E., "Ares I Vehicle Computed Turbulent Ascent Aerodynamic Data Development and Analysis," *Journal of Spacecraft and Rockets*, Vol. 49, No. 4, 2012, pp. 596–608.
https://doi.org/10.2514/1.A32112

[22] Abdol-Hamid, K. S., and Ghaffari, F., "Error Estimates of the Ares I Computed Turbulent Ascent Longitudinal Aerodynamic Analysis," *Journal of Spacecraft and Rockets*, Vol. 49, No. 4, 2012, pp. 609–616.
https://doi.org/10.2514/1.A32143

[23] Krist, S. E., and Ghaffari, F., "Detached Eddy Simulation Results for a Space Launch System Configuration at Liftoff Conditions and Comparison with Experiment," AIAA Paper 2015-0776, 2015.
https://doi.org/10.2514/6.2015-0776

[24] Helden Aerospace, https://heldenaero.com/heldenmesh/ [retrieved 20 Oct. 2023].

J. Pinier
Associate Editor